

Investigation of some physical properties of ZnO nanofilms synthesized by micro-droplet technique

Rajesh Satapathy, *Department of Basic Science, Aryan Institute of Engineering & Technology, Bhubaneswar*

Samaresh Mishra, *Department of Basic Science, Raajdhani Engineering College, Bhubaneswar*

Dr. Paramananda Jena, *Department of Basic Science, NM Institute of Engineering & Technology, Bhubaneswar*

ABSTRACT:

*In this paper, ZnO nanocrystals were synthesized using a simple micro-droplets technique from a solution prepared by dissolving zinc acetate di-hydrate [Zn(CH₃COO)₂, 2H₂O] in methanol. Microdroplets were deposited on glass substrates heated at 100 °C, the obtained samples of ZnO films were investigated by XRD, AES, AFM, ellipsometry and PL. XRD patterns reveal the wurtzite structure of ZnO where the lattice parameters *a* and *c*, calculated from XRD signals, show a nanometric character of ZnO nanoparticles. The chemical composition of ZnO film surfaces was verified by Auger electron spectroscopy (AES). From Auger signals, oxygen (O-KLL) and zinc (Zn-LMM) Auger transitions indicate well the presence of Zn-O bonding. The surface topography of the samples was measured by atomic force microscopy (AFM) where ZnO nanoparticles of average size ranging between 20 and 80 nm were determined. Some optical properties as dielectric constants, refractive index, extinction coefficient as well as the optical band gap were determined from ellipsometry analysis. The dispersion of the refractive index was discussed in terms of both Cauchy parameters and Wemple & Di-Dominico single oscillator model. The photoluminescence (PL) measurements exhibited two emission peaks. The first at 338 nm, corresponding to the band gap of ZnO, is due to excitonic emission while the second around 400 nm, is attributed to the single ionized oxygen vacancies.*

Keywords: ZnO nanoparticles Micro droplets technique AFM Auger spectroscopy Ellipsometry Photoluminescence (PL)

I. INTRODUCTION

Zinc oxide (ZnO) is a material which is very familiar to scientists because it is well known for its excellent physical properties as ultra violet absorbance, piezoelectricity and luminescence at high temperatures. We can count thousands of papers dating back as early as 1935 [1]. More recently, ZnO has again entered the scientific spotlight, this time for its semiconducting properties. ZnO is a semiconductor with interesting characteristics such as a wide and direct bandgap (3.37 eV at room temperature) and a larger exciton binding energy (60 meV) [2,3]. It is a very interesting material for its large applications in many technological fields for its useful properties (optical, electrical, mechanical, chemical..). A considerable research interest in ZnO was performed due to many potential applications particularly in short wavelength for optoelectronic devices operating in the blue and ultraviolet (UV) region such as light-emitting diodes (LED) [4] and gas-sensing applications [5].

Today, the research is focused on the nanostructured ZnO because there is a high surface-to-volume ratio and show enhanced chemical stability and electrical performances [6,7].

Several chemical and physical methods have been used for the preparation of ZnO thin films nanostructured such as MOCVD [8], chemical vapor transport (CVT) [9], spray pyrolysis [10–12], sputtering [13], laser ablation [14,15].

The purpose of this paper is to provide a simple chemical synthesis route of ZnO nanofilms. This technique called “micro-droplets technique” is low cost and easy to implement. It is based on the deposit of microdroplets on heated glass substrates. The detail of this technique is described in the following paragraph.

Experimental part

ZnO nanofilms preparation

ZnO nanofilms were obtained by micro-droplets route. The principle of this method is to prepare a solution by dissolving 10–2 M of zinc acetate di-hydrate [Zn(CH₃COO)₂, 2H₂O] in a beaker containing

150 ml of methanol. Microdroplets of 0.05 ml of volume dropped with pipette from the solution were deposited on glass substrates heated at 100 °C. Before depositing the drops and in order to remove the air contamination, glass substrates of dimension 1 cm × 1 cm × 0.2 cm were cleaned in ultrasonic bath for several cycles, rinsed in de-ionized water and finished in air dried. ZnO samples were obtained by dropping the solution 20 and 30 times. The samples, named #S1 (for 20 drops) and #S2 (for 30 drops), were studied by XRD, AES, AFM, ellipsometry and photoluminescence (PL) techniques.

Characterization techniques

The crystallographic structures of the samples #S1 and #S2 were examined by X-ray diffraction apparatus using Cu-Kα radiation ($k = 1.54 \text{ \AA}$). DRX results are interpreted in the following structural properties. The chemical composition of ZnO samples was controlled by Auger electron spectroscopy (AES). Auger spectroscopy analyses were performed in ultrahigh vacuum (10^{-9} torr) using primary electron energy beam of 2 keV for samples excitation and cylindrical mirror analyzer (CMA) for Auger spectra acquisition in derivative mode (dN/dE). We comment Auger results in the AES analysis. The surface morphology and the grain size of ZnO films were studied with Bruker Dimension Edge Model atomic force microscope. The AFM images obtained in tapping mode are discussed in the surface morphology and AFM characterization.

The optical properties were studied by ellipsometry in the wavelength range 250–800 nm. The photoluminescence (PL) measurements were used as complement of optical characterization. The discussion of optical results is presented in the optical properties of the paragraph 3.

II. RESULTS AND DISCUSSION

Structural properties

X-ray diffraction patterns of samples #S1 and #S2 are illustrated in Fig. 1. From this figure, ZnO diffraction peaks are well defined and are indexed as (010), (002), (011), (012), (110) and (013) orientations corresponding to hexagonal (wurtzite) phase according to JCPDS 036-1451 card. (002) peak is the most intense; it can be seen with a preferential orientation along c-axis perpendicular to the sample surface. In other hand, the XRD spectra show a broad diffraction peaks suggesting that the prepared ZnO nanofilms are composed by nanocrystallites. As the structure is hexagonal, the lattice parameters a and c may be deduced from the relation (1). In fact, in the hexagonal structure, the interplanar dis-

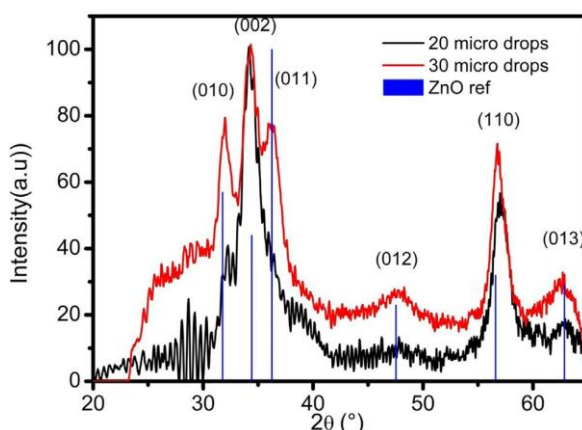


Fig. 1. DRX spectra of ZnO nanofilms.

tance d is linked to the lattice parameters a and c and the Miller indices h, k, l by the relationship (2) [16,17];

$$\frac{1}{d^2} = \frac{4}{3} \left(\frac{h^2 + k^2}{a^2} + \frac{l^2}{c^2} \right)$$

$$d = \frac{1}{\sqrt{\frac{4}{3} \left(\frac{h^2 + k^2}{a^2} + \frac{l^2}{c^2} \right)}}$$

is calculated by using Bragg relation

$$2d \sin \theta = n\lambda$$

$$\frac{1}{d^2} = \frac{4}{3} \left(\frac{h^2 + k^2}{a^2} + \frac{l^2}{c^2} \right)$$

where n is the order of diffraction (often $n = 1$) and k is the X-ray wavelength.

The calculated values of lattice parameters are resumed in Table 1 and agree well with those reported elsewhere [19–21].

On the other hand, it is known that in the compactness *hcp* phase, the *c-to-a* ratio is 1.602, the obtained difference in our case can be attributed to the nanometric character of the crystallites and defects. Regarding the width of the diffraction peaks, a study of structural parameters such as the size of the crystallites, the stress and dislocations for both (002) and (110) orientations were made from the experimental data of X-ray diffraction. These parameters were calculated from the following relations [22–27]:

$$D = \frac{k \cdot \lambda}{\beta_1 \cos(\theta)} \quad (3)$$

$$\xi = \frac{\beta_1}{4 \tan(\theta)} \quad (4)$$

$$\delta = \frac{1}{D^2} \quad (5)$$

where $k = 0.90$ is the Scherrer constant, $k = 1.54 \text{ \AA}$ is the wavelength of Cu-K α radiation, b is the full width at half maximum (FWHM) and h is the Bragg's diffraction angle.

The calculated values of these structural parameters are presented in Tables 2 and 3.

From the calculation of structural constants, it would seem that ZnO oxide contains some defects such as high values of both dislocation and strain. This observation is coherent with those previously discussed and indeed the prepared thin layers are formed by nano-ZnO crystals.

It is also noted that the crystallites size of the thin film of sample #S2 is greater than those in sample #S1. For sample #S2, the crystallites are welded together. In fact, when the number of the drops increases, the crystallites of ZnO agglomerate and can be modeled by a spider effect. The kinetics of this effect can be described by the following steps:

At first there is formation of a few stitches of ZnO (Fig. 2(a)) which agglomerate (Fig. 2(b)) and form crystallites (Fig. 2(c)) and at the end we observe the formation of ZnO nanocrystallites. The size depends on the number of deposited microdrops as indicated in Fig. 2(d).

AES analysis

Fig. 3 shows Auger spectrum of ZnO films which the same of the samples #S1 and #S2. As indicated in this figure, the spectrum is

Table 1
Lattice parameters of ZnO microdropped thin films determined from XRD signals.

	a (Å)	c (Å)	c/a
Sample #S1	3.2231	5.2257	1.621
Sample #S2	3.2367	5.2256	1.614

Table 2
Average values of Grain size, dislocation density and microstrain for sample #S1.

	D (nm)	e (10^{-4})	d (10^{14} line/m ²)
(002)	11.76	99.94	72.31
(110)	10.69	67.80	87.47

Table 3
Average values of Grain size, dislocation density and microstrain for sample #S2.

	D (nm)	e (10^{-4})	d (10^{14} line/m ²)
(002)	17.11	68.68	34.15
(110)	15.22	47.82	43.16

composed by three peaks corresponding respectively to C-KLL, O- KLL and Zn-LMM Auger transitions.

The presence of carbon is due to surface residual contamination which is usually present on surface samples and often combined to oxygen to form C-O molecules which probably originates in the decomposition of the methanol used for the solution. These molecules are easily eliminated in situ using argon ions bombardment of energy of 500 eV. As shown in Fig. 4 and after Ar⁺ ions surface cleaning, Auger spectrum shows no traces of carbon.

From the spectrum in Fig. 4, the ratio calculated from the peak to peak height intensities of Auger transitions of Zn-LMM and O- KLL (I_{Zn-LMM}/I_{O-KLL}) is slightly different to 1. This result indicates

well the formation of zinc oxide but not quite stoichiometric. The films are composed of ZnO_x where $x < 1$. This result is due to a deficiency of Zn in ZnO films.

This deficiency could be the result of mechanisms that intervene during the growth of ZnO nanofilm: Indeed, one could invoke the occupation of the interstitial sites by Zn in the lattice of ZnO. It may be also due to the presence of some dispersed residual phases of Zn(OH₂) hydroxide on sample surface which under Ar⁺ bombardment effect Zn(OH₂) is decomposed into small Zn-O nanocrystallites and release some zinc atoms. This lack of zinc in ZnO is then required for gas sensors and magnetic properties of such oxides thin films.

Surface morphology and AFM characterization

AFM images of ZnO films are shown in Fig. 5. The images were treated using WSXM (Windows Scanning Microscope, X is standing for either STM or AFM) software [28]. AFM images in Fig. 5 (a) and (c) indicate the morphology of ZnO films in 2D and 3D. The surface of samples #S1 and #S2 presents a morphology formed by small grains. The surface is homogeneous with slight roughness due to the coordination of ZnO nanoparticles between them.

As shown in Fig. 5(d) and (f), on a zoomed scale (1 μm 1 μm) in 2D and 3D respectively, the grains are rounds and are assembled to form ZnO nanolayer with a clear grain boundaries.

The profile presented in Fig. 5(b) shows the variation of the height Z varies where the maximum is at 12 nm. The profile is

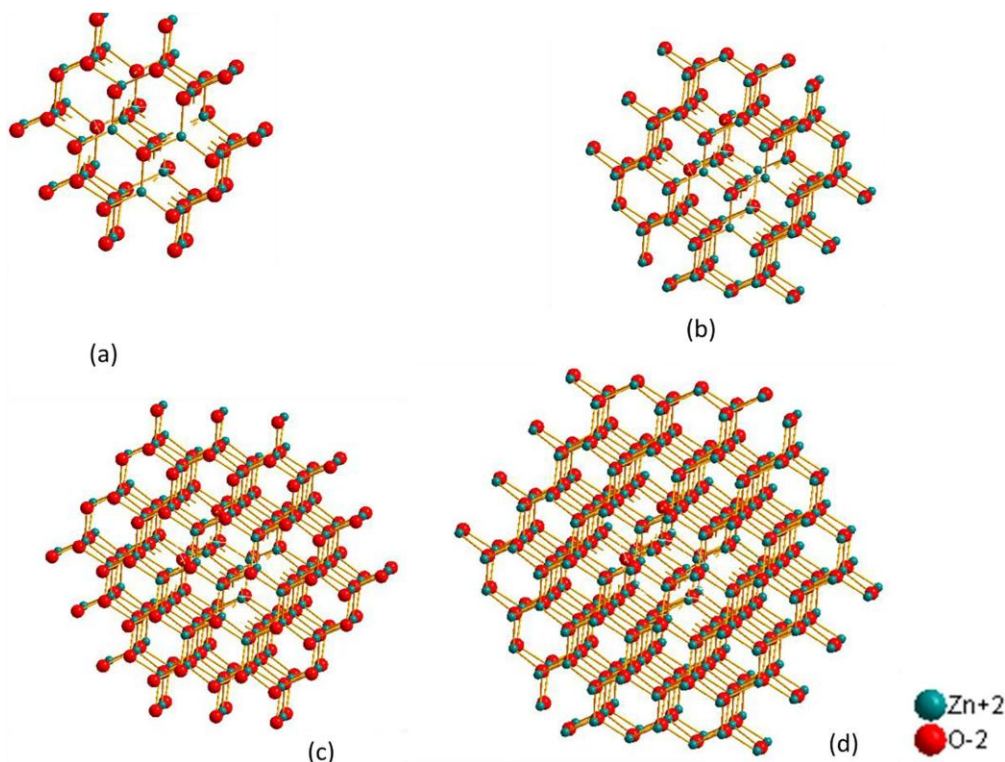


Fig. 2. Descriptive diagram of crystallites formation by spider's effect.

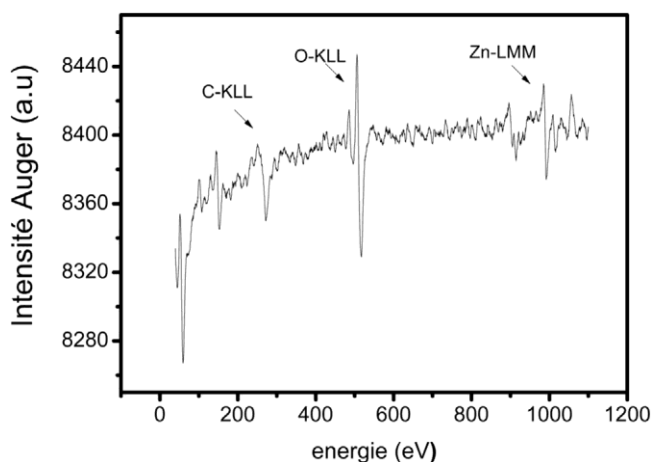


Fig. 3. Auger spectrum of ZnO nanofilms before Ar⁺ ions cleaning in auger chamber.

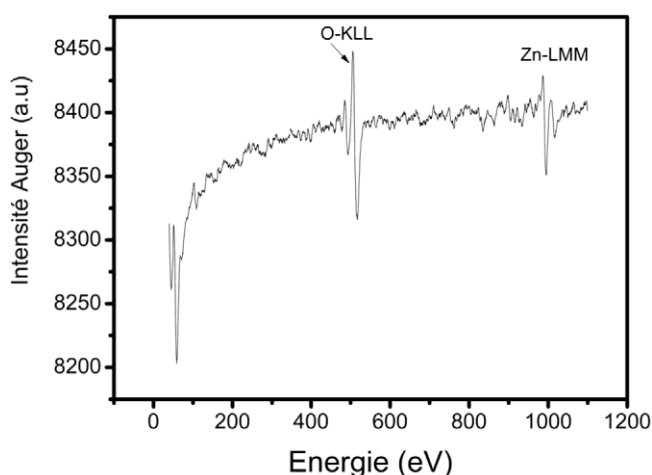


Fig. 4. Auger spectra of ZnO nanofilms after Ar⁺ bombardment.

depending on the grain size as shown in Fig. 5(e). From this profile, it can be deduced that the largest grain has a size of about 80 nm.

Optical properties

Ellipsometry characterization

Ellipsometric measurements are described by two important parameters W and D which appear in the following relation [29]:

$$\frac{r_p}{r_s} = \frac{1}{4} \tan W e^{iD} \quad (6)$$

where $\tan W = \frac{|r_p|}{|r_s|}$ is the amplitude ratio upon reflection and $D = \delta_p - \delta_s$ is the phase shift difference.

In Fig. 6, we show the plot of $\tan(W)$ and $\cos(D)$ of ZnO thin films

It is found that these curves show two behaviors for a low wavelengths (<350 nm) which corresponds to the absorption zone and the other for high wavelengths (>380 nm) which corresponds to the area of transparency. These two zones are separated by a passage zone which is for a minimum in the vicinity of 360 nm for the sample #S1 and 350 nm for the sample #S2. The maximum is located at 430 nm for the sample #S1, for the sample #S2 it is situated at 380 nm.

This ratio (q) is related to the complex dielectric function, $\epsilon = \epsilon_1 + i\epsilon_2$, by the following relation [30,31]:

$$e_1 = \frac{1}{4} \sin^2 \theta_i \left[\frac{1 - \frac{q^2}{\delta^2}}{1 + \frac{q^2}{\delta^2}} \right] \quad (8)$$

The variation of the real (e_1) and imaginary (e_2) parts of the dielectric constant of different ZnO grown from 20 and 30 drops is illustrated in the Fig. 7(a) and (b) respectively.

From this dielectric constant study, it is clear that the dispersion of real part decreases with the wavelength and the imaginary part is high in the UV range, its value becomes lower in the visible domains. Also, these figures reveal that the values of the real part are higher than the imaginary one, which shows the transparency of these thin films.

As verified by calculation methods, Figs. 8 and 9 show the experimental and simulated plots of $\tan(\delta)$ and $\cos(\delta)$.

It is clear from this study that the experimental and simulated values of $\tan(\delta)$ and $\cos(\delta)$ are very close and give reliability to the optical parameters values of these thin layers.

To confirm these observations, a further study of the mean values and standard deviation was carried out. Figs. 10 and 11 show the variations in the average between experimental and simulated values and the standard deviation. It is clear that the experimental and simulated values are very close and are substantially equal to their average values. In addition the standard deviation is zero, which proves the consistency between simulation and experimental values.

The optical coefficients $n(k)$ and $k(k)$, for a wavelength k ranging from 250 to 800 nm, have been calculated using optical experimental measurements.

The dispersion of the refractive index $n(k)$ and the extinction coefficient $k(k)$, were operated by means of the following relations:

$$e_1 = \frac{1}{4} \left[\frac{\delta^2 - k^2}{\delta^2 + k^2} \right] \quad (9)$$

$$e_2 = \frac{1}{4} \left[\frac{2\delta k}{\delta^2 + k^2} \right] \quad (10)$$

$$e_2 = \frac{1}{4} \left[\frac{2n\delta k}{\delta^2 + k^2} \right] \quad (11)$$

The plots of $n(k)$ and $k(k)$ are presented in Fig. 12(a) and (b). The extinction coefficient k values decreases up to certain value of wavelength and then increase.

It is found that the extinction coefficient k spectra, presented in Fig. 12(a), shows an obvious decrease versus wavelength till to reach low values in the visible and near infra red range. This confirms their transparent character and the ability to use ZnO as optical windows.

Nevertheless, the dispersion of the refractive index is fitted by Cauchy formula [32]:

$$n = A + \frac{B}{\lambda^2} + \frac{C}{\lambda^4} \quad (12)$$

where A , B and C are the Cauchy's parameters and k is the wavelength. Cauchy's parameters values are summarized in Table 4.

However, the optical dispersion parameters E_0 and E_d , derived

from the real part of the final refractive index are evaluated according to single effective oscillator model proposed by Wemple and Di-Domenico [33,34]. It is well known from the dispersion theory that in the region of low absorption the refractive index n is given in a single-oscillator model by the expression:

$$n^2 = 1 + \frac{E_0 E_d}{E_0 - E^2} \quad (13)$$

where $E = h\nu$ is the incident photon energy, E_0 is the single-

oscillator energy and E_d is the dispersion energy. By plotting $(n^2 - 1)^{-1}$ versus $(ht)^2$ and filling the data to a straight line, E_0 and E_d can be determined both from the intercept (E_0/E_d) and the slope ($-1/E_0E_d$). Their values are listed in Table 4.

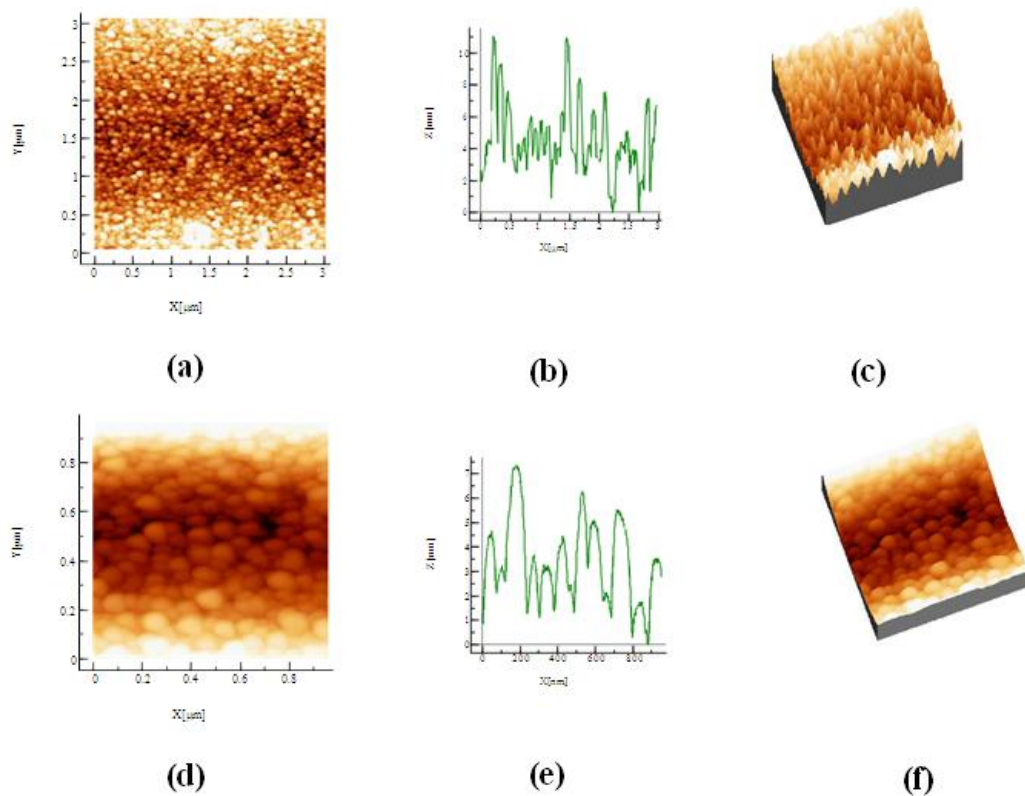


Fig. 5. 2D and 3D AFM images of ZnO microdropped nanofilms (a) image 3 μm × 3 μm, (b) rough profile, (c) 3 D image, (d) Zoomed image 1 μm × 1 μm, (e) rough profile, (f) 3D image.

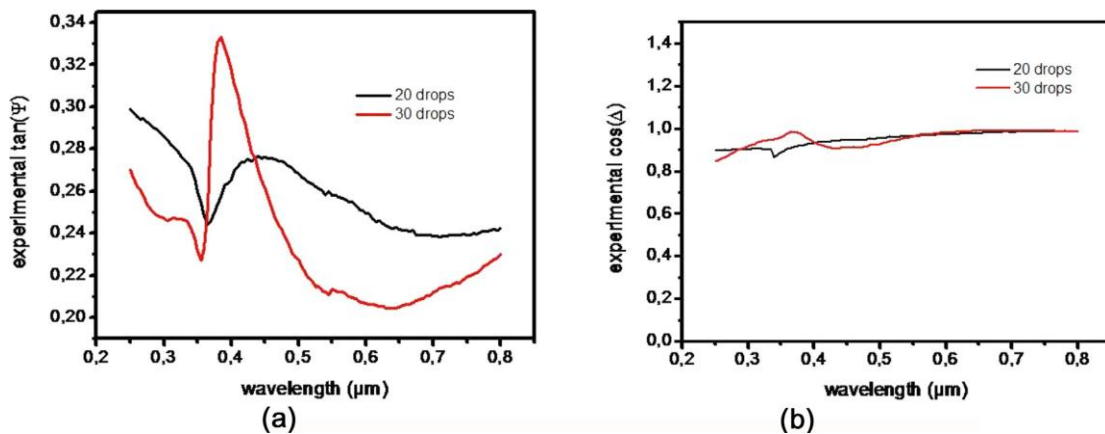


Fig. 6. Plot of $\tan(\psi)$ (a) and $\cos(D)$ (b) of ZnO microdropped nanofilms.

Finally, the absorption coefficient is deduced in this study by the relation [31]:

$$a_{\frac{1}{4}} = \frac{4Pk}{k}$$

013p

As ZnO is a direct band gap material, the optical band gap energy of film was determined using the equation [35]:

$$ahm \frac{1}{4} B hm - E_g^{1-2}$$

014p

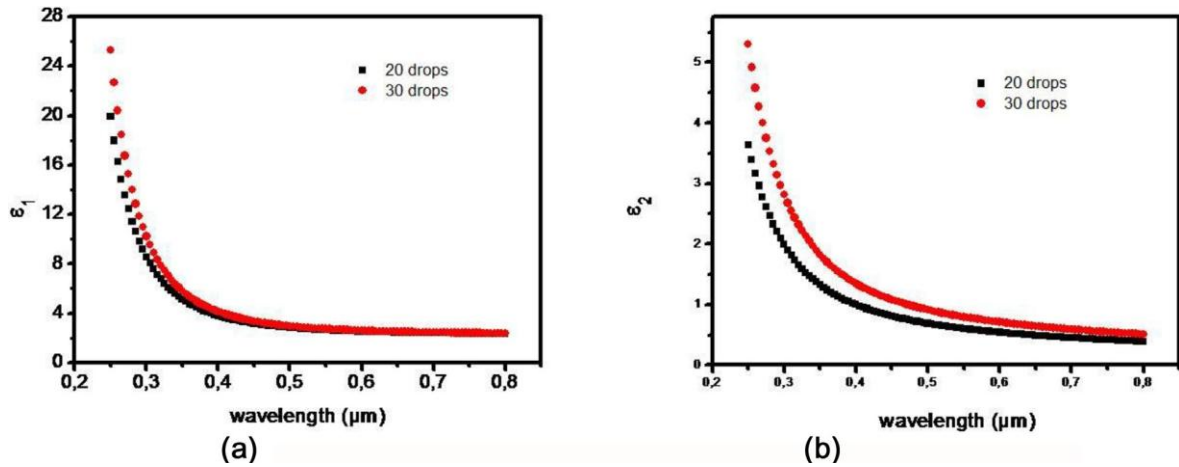


Fig. 7. Plot of ϵ_1 (a) and ϵ_2 (b).

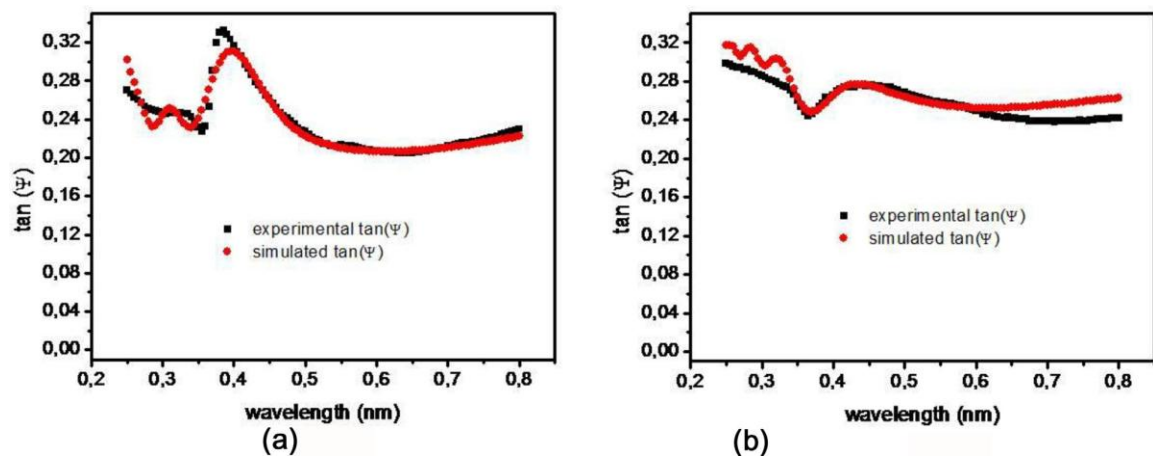


Fig. 8. Experimental and simulated plots of $\tan(\Psi)$: (a) for sample #S1, (b) for #S2.

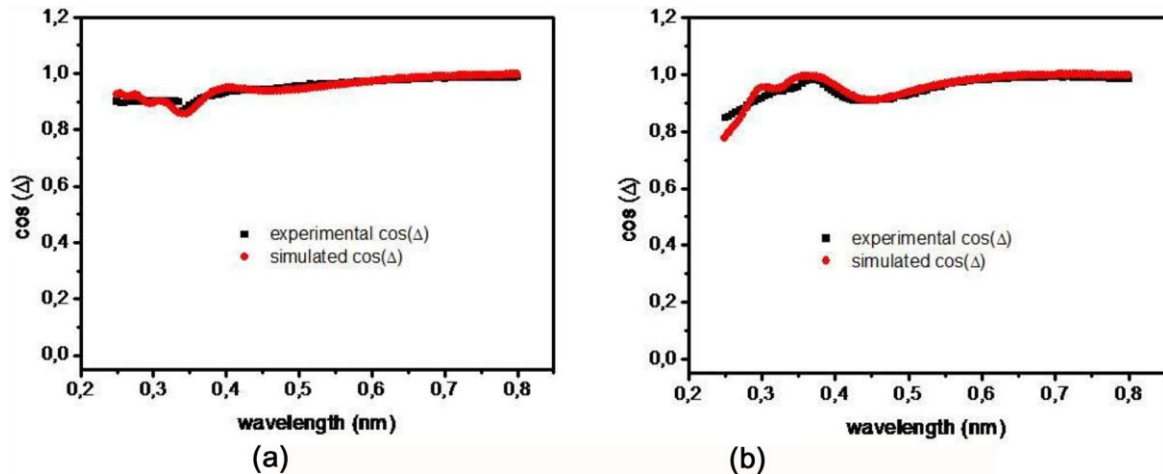


Fig. 9. Experimental and simulated plots of $\cos(\Delta)$: (a) for (a) for sample #S1, (b) for #S2.

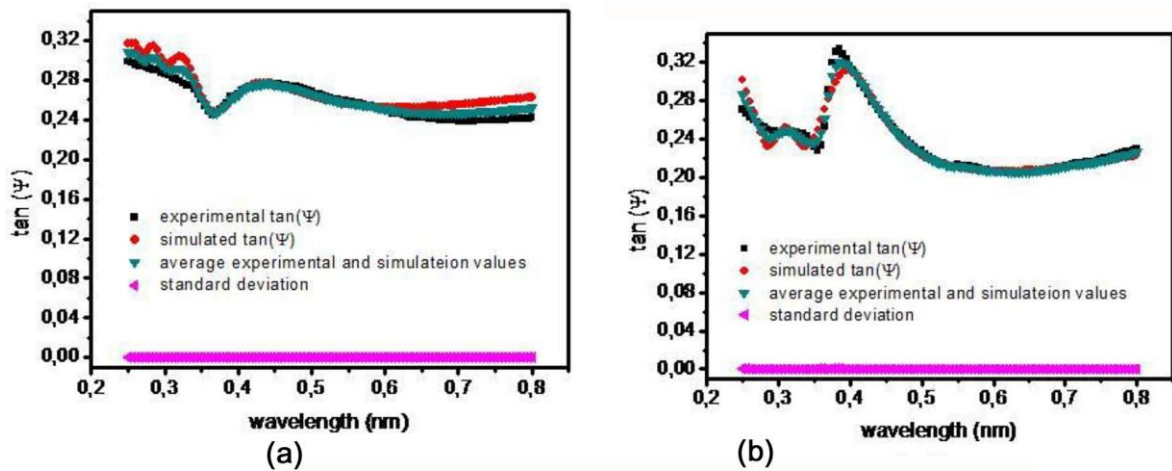


Fig. 10. Experimental, simulated, average experimental and standard deviation plot of $\tan(\Psi)$: (a) for sample #S1, (b) for #S2.

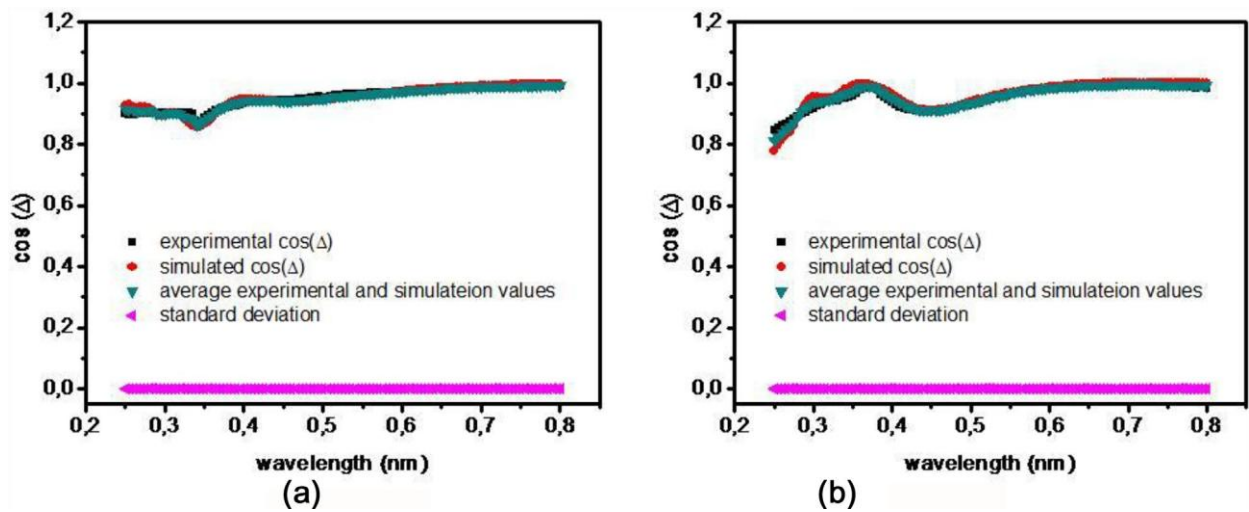


Fig. 11. Experimental, simulated, average experimental and standard deviation plot of $\cos(\Delta)$: (a) for sample #S1, (b) for #S2.

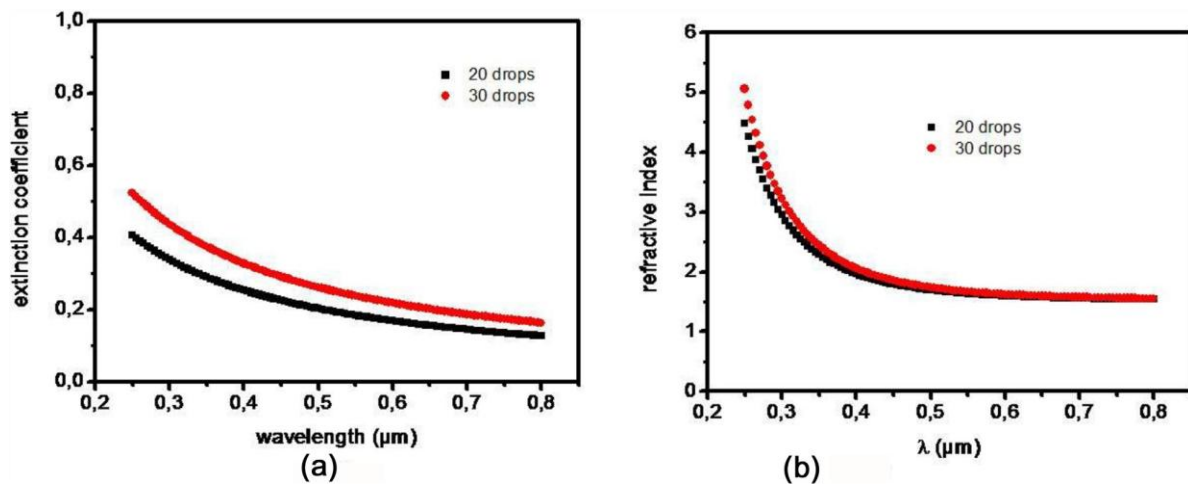


Fig. 12. Extinction coefficient (a) and refractive index variations of refractive index with wavelength.

Table 4

Values of Cauchy and Wemple and Di-Dominico parameters of ZnO microdropped thin films.

	A	B (mm ²)	C (mm ⁴)	E ₀ (eV)	E _d (eV)
Sample #S1	1.5071	0.00104	0.0115	3.92764	4.41487
Sample #S2	1.51804	2.7338E-5	0.01383	3.77469	4.33305

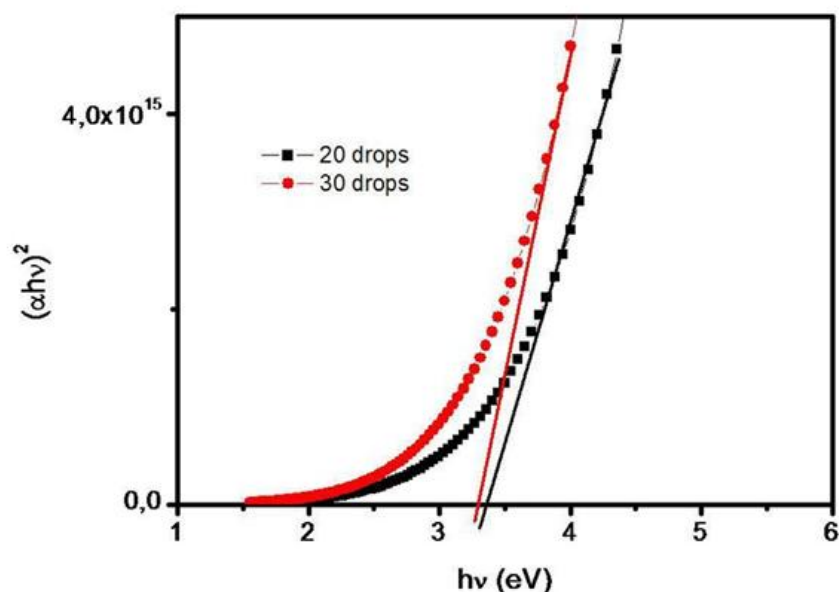


Fig. 13. Plot of $(\alpha h\nu)^2$ versus photon energy of ZnO microdropped thin films.

Table 5
Optical band gap values.

	E _g (eV)
Sample #S1	3.34
Sample #S2	3.29

where E_g is the optical band gap, $h\nu$ is the incident photon energy and B is a constant. Therefore, the optical band gap is obtained using Tauc's plot by plotting $(\alpha h\nu)^2$ versus $(h\nu)$ and extrapolating the linear portion to find the intercept with energy axis (Fig. 13). The calculated values of optical band gap are indicated in Table 5.

We observe the effect of the micro-drops number on the optical band gap. The high value observed in the film prepared with 20 microdrops is probably due to the defects and the non-stoichiometric character mentioned above.

Table 6
Positions of PL peaks of ZnO microdropped thin films.

	1st position Peak (nm)	2nd position Peak (nm)	3rd position peak (nm)	4th position peak (nm)
Sample #S1	338	391	480	690
Sample #S2	340	392	450	700

Photoluminescence study

In order to complete the optical investigation of ZnO nanofilms, photoluminescence measurements (PL) working at room temperature, were performed in the wavelength range 200–900 nm. PL excitation was He/Cd laser light of 325 nm wavelength.

PL spectra and their deconvolutions (Gaussian analysis) are shown in Fig. 14. In the Table 6, we

present the peaks positions. From this figure, we can discuss the following points:

1. The deconvoluted peak around 391 nm (3.18 eV), originated from the exciton recombination corresponds to the near-band edge (NBE) transition of ZnO [36].
2. According to several authors [37–39], the broad blue emission detected at 480 nm is due to the exciton recombination between the electron localized at the interstitial zinc (Zn_i) and the holes in the valence band.
3. The large red emission peak observed at 690 nm is probably related to stoichiometry defects in the prepared thin films which have been discussed in Auger spectroscopy analysis paragraph.
4. The emission at 338 nm is interpreted as due to the some $Zn(OH)_2$ and the effect of the substrate which confirms the nano-metric character of the deposited layers

III. SUMMARY

In this work, we have reported some physical properties of ZnO nanofilms prepared by microdroplets technique. X-ray diffraction analysis shows that the prepared film is mainly formed by hexagonal wurtzite ZnO phase. The chemical composition of the ZnO

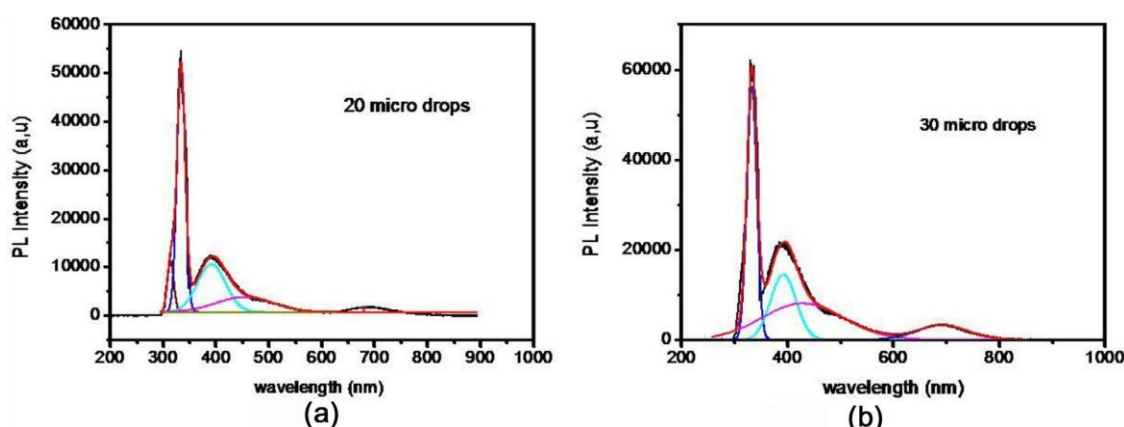


Fig. 14. Room temperature PL spectra of ZnO microdropped thin films.

deposits is confirmed by Auger electrons spectroscopy (AES) analysis. Auger peaks of zinc and oxygen show a ratio of intensities (I_{Zn-LMM}/I_{O-KLL}) slightly greater than 1 let us to think that there is some deficiencies of zinc.

Ellipsometric measurements were used to investigate the optical properties of ZnO nanofilms in terms of dielectric function, extinction coefficient and refractive indexes as well as the optical band gap. Wemple-Di Domenico single oscillator model and Cauchy parameters have been determined from the calculating refractive index in low absorption range. The optical measurements are completed by photoluminescence (PL) where the emission peak of ZnO compound is detected. Further studies are in progress in order to determine electrical and thermal properties of ZnO prepared by micro-droplets method.

ACKNOWLEDGEMENTS

The authors thank Prof. D. Tonneau and B. Aufray from Aix-Marseille University (France) for Auger and photoluminescence analysis and Vasile Heresanu for DRX experiments. They also thank a lot the Algerian-French cooperation through the tassili 14MDU915 project for the funding support.

REFERENCES

- [1]. Bunn CW. The lattice dimension of zinc oxide. Proc Phys Soc 1935;47:835.
- [2]. Peng W, Qu S, Cong G, Wang Z. Cryst Growth Des 2006;6:1518.
- [3]. Ivill M, Pearton SJ, Norton DP, Kelly J, Hebard AF. J Appl Phys 2005;97:053904.
- [4]. Wang HQ, Koshizaki N, Li L, Jia LC, Kawaguchi K, Li XY, Pyatenko A, Swiatkowska-Warkocka Z, Bando Y, Golberg D. Adv Mater 2011;23:1865.
- [5]. Subramanyam TK, Srinivasulu BN, Uthanna S. Cryst Res Technol 2000;35(10):1193–202.
- [6]. Skorenko K, Bernier RT, Liu J, Galusha B, Goroleski F, Hughes BP, Bernier WE, Jones WE. J Dyes Pigm 2016;131:69.
- [7]. Chiba H, Mori T, Okuda S, Washio K. Thin Solid Films 2014;557:203.

- [8]. Sanga B, Nagoyab Y, Kushiyab K, Yamase O. Sol Energy Mater Sol Cells 2003;75:179.
- [9]. Fu Q, Hu L, Yu D, Sun J, Zhang H, Huo B, Zhao Z. Mater Lett 2009;63:316.
- [10]. Shimomura T, Kim D, Nakayama M. J Lumin 2005;112:191.

- Henley SJ, Ashfold MNR, Cherns D. *Surface Coat Technol* 2004;177–178:271.
- [11]. Dinescu M, Verardi P. *Appl Surf Sci* 1996;106:149.
- [12]. van Heerden JL, Swanepoel R. *Thin Solid Films* 1997;1–2:72.
- [13]. Seeber WT, Abou-Helal MO, Bartha S, Beil D, Ho Eche T, Afify HH, Demian SE. *Mater Sci Semicond Process* 1999;2:45.
- [14]. Ashour A, Kaïd MA, El-Sayed NZ, Ibrahim AA. *Appl Surface Sci* 2006;252:7844.
- [15]. Peng LP, Fang L, Yang XF, Li YJ, Huang QL, Wu F, Kong CY. *J Alloys Compd* 2009;484:575.
- [16]. Boukhachem A, Ouni B, Karyaoui M, Madani A, Chtourou R, Amlouk M. *Mater Sci Semicond Process* 2012;15:282.
- [17]. Lupan O, Pauporté T, Chow L, Viana B, Pellé F, Ono LK, Roldan Cuenya B, Heinrich H. *Appl Surface Sci* 2010;256:1895.
- [18]. Kamoun O, Boukhachem A, Yumak A, Petkova P, Boubaker K, Amlouk M. *Mater Sci Semicond Process* 2016;43:8.
- [19]. Mrabet C, Kamoun O, Boukhachem A, Amlouk M, Manoubi T. *J Alloys Compd* 2015;648:826.
- [20]. Suwanboon S, Amornpitoksuk P, Sukolrat A, Muensit N. *Ceram Int* 2013;39:2811.
- [21]. Loukil A, Boukhachem A, Ben Amor M, Ghamnia M, Raouadi K. *Ceram Int* 2016;42:8274.
- [22]. Boukhachem A, Bouzidi C, Boughalmi R, Ouerteni R, Kahlaoui M, Ouni B, Elhouichet H, Amlouk M. *Ceram Int* 2014;40:13427.
- [23]. Kamoun O, Boukhachem A, Mrabet C, Yumak A, Petkova P, Boubaker K, Amlouk M. *Bull Mater Sci* 2016;39:777.
- [24]. M. Bull Mater Sci 2016;39:777.
- [25]. Tripathi R, Kumar A, Bharti C, Sinha TP. *Curr App Phys* 2010;10:676.
- [26]. Junaid S, Qazi S, Rennie Adrian R, Cockcroft Jeremy K, Vickers Martin. *J Colloid Interface Sci* 2009;338:105.
- [27]. Sahay PP, Nath RK. *Sens Actuators B* 2008;134:654.
- [28]. Horcas I, Fernandez R, Gomez-Rodriguez JM, Colchero J, Gomez-Herrero J, Baro AM. *Rev Sci Instrum* 2007;78:013702.
- [29]. Azzam RMA, Bashara NM. *Ellipsometry and polarized light*. New York: North-Holland; 1977.
- [30]. Sampath U, Kim H, Kim D-G, Kim Y-C, Song M. *Sensors* 2015;15:18229.
- [31]. Sdiri N, Boukhachem A, Dhahri E. *Ceram Silik* 2012;56(2):95.
- [32]. Kumari N, Krupanidhi SB, Varma KBR. *Mater Res Bull* 2010;45:465.
- [33]. Aspnes DE. *J Optical Soc Am* 1980;70:1275.
- [34]. Karyaoui M, Mhamdi A, Kaouach H, Labidi A, Boukhachem A, Boubaker K, Amlouk M, Chtourou R. *Mater Sci Semicond Process* 2015;30:255.
- [35]. Wemple SH, DiDomenico M. *J Chem Phys* 1977;67:2151.
- [36]. DiDomenico M, Eibschütz M, Guggenheim HJ, Camlibel I. *Solid State Commun* 1969;7(16):1119.
- [37]. Belgacem S, Bennaceur R. *Rev Phys Appl* 1990;25:1245.
- [38]. Pankove JJ. *Optical processes in semiconductors*. Englewood Cliffs, NJ: Prentice-Hall Inc; 1971.
- [39]. Li J, Xu J, Xu Q. *J Alloys Compd* 2012;542:151.